

Article

Formic Acid Oxidation on Pd Thin Film Coated Au Nanocrystals

Yongan Tang ^{1,†}  and Shouzhong Zou ^{2,*,†}¹ DOD Technologies Inc., Cary, IL 60013, USA; tangy3@miamioh.edu² Department of Chemistry, American University, Washington, DC 20016, USA

* Correspondence: szou@american.edu

† Department of Chemistry and Biochemistry, Miami University, Oxford, OH 45056, USA.

Received: 5 April 2019; Accepted: 6 May 2019; Published: 10 May 2019



Abstract: Cubic, octahedral, and rhombic dodecahedral gold nanocrystals enclosed by {100}, {111}, and {110} facets, respectively, were prepared by a seed-mediated growth method at the room temperature. Palladium thin films were coated on these Au nanocrystals by a redox replacement approach to explore their catalytic activities. It is revealed that formic acid and carbon monoxide oxidation in 0.1 M HClO₄ on Au nanocrystals coated with one monolayer (ML) of Pd are facet-dependent and resemble those obtained from corresponding Pd single crystals and Pd films deposited on bulk Au single crystals, suggesting epitaxial growth of Pd overlayers on the Au nanocrystal surfaces. As the Pd film thickness increased, formic acid oxidation current density decreased and the CO oxidation potential moved to more negative. The catalytic activity remained largely unchanged after 3–5 MLs of Pd deposition. The specific adsorption of (bi)sulfate was shown to hinder the formic acid oxidation and the effect decreased with the increasing Pd film thickness. These observations were explained in the framework of the d-band theory. This study highlights the feasibility of engineering high-performance catalysts through deposition of catalytically active metal thin films on facet-controlled inert nanocrystals.

Keywords: formic acid oxidation; Au nanocrystals; Pd thin films; electrocatalysis; d-band theory

1. Introduction

Direct formic acid fuel cells (DFAFCs) have attracted much attention in the past decade because they have the advantages of high power density, fast oxidation kinetics, high theoretical cell potential, and mild fuel crossover as compared to direct methanol fuel cells [1–5]. As the anode reaction of DFAFCs, electrooxidation of formic acid has been extensively studied [2,5]. Although the nature of the reactive intermediate is under active debate, it is generally accepted that there are two reaction pathways in formic acid oxidation (FAO) [2,6]. The direct pathway (dehydrogenation) involves the adsorption of reactive intermediates and their direct oxidation to carbon dioxide, while the indirect pathway goes through the dehydration of formic acid and forms strongly adsorbed carbon monoxide (CO_{ads}) that poisons catalysts [2,6]. It has been long recognized that the direct pathway is dominant on Pd while the indirect pathway is more prevalent on Pt, which suggests that Pd is a better catalyst than Pt for DFAFCs [6,7]. Indeed, using unsupported and carbon-supported Pd as anode catalysts in DFAFCs, Masel and coworkers obtained better fuel cell performance than Pt-based catalysts at high power densities [8,9]. Despite the higher activity observed on Pd, a significant performance decay was observed after only a few hours of operation [9]. Different adsorbed species, including CO_{ads}, have been proposed to explain the deactivation of the Pd catalysts [2]. In addition, it has been shown that Pd dissolution occurred in an acidic media, resulting in a decreased active surface area [10,11].

Significant efforts have been devoted to develop Pd-based catalysts with high activity as well as long-term durability and stability [2,5,12]. A commonly employed approach is to introduce a second metal either to form an alloy with Pd or as a support for Pd overlayers. Of particular interest in the present work is the Pd–Au combination. Zhou and Lee reported that Au core Pd shell (Au@Pd) nanoparticles showed significantly improved FAO activity and durability, which was attributed to the Au and Pd electronic interactions [13]. More detailed studies by others revealed that the improved FAO activity depends on the Au/Pd ratio [14] and the degree of alloying [15]. Lee et al. found that FAO activity and durability of Pd₃Au nanoparticles can be significantly improved by increasing the surface Pd content through CO-induced surface aggregation [16]. Hong et al. studied FAO on structurally well-controlled PdAu nano-octahedra, and revealed that PdAu alloy octahedra are about 30% more active than similar size Au@Pd octahedra, but both are more active than pure Pd octahedra [17]. By using a seed-mediated growth method, Fermín and coworkers prepared Au@Pd nanoparticles with varying Pd shell thickness from 1 to 10 nm [18]. FAO activity on these core-shell particles was shown to increase with the Pd shell thickness, which was attributed to the lattice strain effect. More recently, by combining differential electrochemical mass spectrometry and in situ Fourier transform infrared spectroscopy with the density functional theory (DFT) calculations, the same group concluded that a faster HCOO_{ads} oxidation step on the thicker Pd shell, induced by the lattice strain effect, might be responsible for the more facile FAO [19].

In addition to the core shell or alloyed nanoparticles, PdAu catalyst can also be prepared by depositing Pd thin films on Au surfaces. Hsu et al. deposited Pd thin films on hollow Au nanospheres through a spontaneous galvanic replacement deposition [20]. Depending on the Pd film's thickness, the Pd-coated Au nanospheres showed enhanced FAO peak current density compared to Pd black, which was ascribed to the electronic coupling between Au and Pd. Obradović and Gojković showed film-thickness-dependent FAO activity on electrochemically deposited Pd films on polycrystalline Au electrodes with the film thickness ranging from 1 to 17 monolayers (MLs) [21]. The maximum peak current density was observed on four ML Pd, but the peak potential is most negative at one ML Pd. All of the Pd films had a higher FAO activity than Pd black, which was attributed to the strain effect from the Au substrate. In an earlier study of FAO on Pd films deposited on various metal surfaces with (111) orientation, Kibler et al. demonstrated nicely the correlation between the d-band center position tuned by the strain effect and the FAO catalytic activity [22]. In their work, Pd monolayer deposited on Au (111) exhibited a higher peak current density than Pd (111), albeit at a higher potential.

One limitation in most of the previous studies of nanoparticles is that the particle surface structure is not controlled and the observed Pd film thickness dependent activity can at least partly arise from the surface structure difference. It has been well-demonstrated that formic acid oxidation is structure-sensitive [7,23–26]. Therefore, controlling the exposed facets of nanoparticles is critical when comparing catalytic activities, and can be used as a tool to improve catalytic performance. In this paper, Pd thin films were deposited on cubic, octahedral, and rhombic dodecahedral (RD) Au nanocrystals that were enclosed by six {100}, eight {111}, and twelve {110} facets, respectively, by a redox replacement approach. The surface-limiting nature of this deposition method ensures the precise control of the film thickness to a monolayer level [27], and pseudomorphic growth of Pd films on Au (111) surface up to several tens of MLs has been demonstrated [28]. The use of nanocrystals with well-defined surface structure minimizes the complication from the surface structural difference of the substrates in film-thickness-dependent studies. Our focus of this study is to explore whether the Pd thin films on Au nanocrystals mimic the electrochemical behaviors of the bulk Pd single crystals and how the FAO activity varies with Pd film thickness. The results reveal that cyclic voltammetric features of hydrogen adsorption/desorption, surface oxidation/reduction, and CO stripping on Au nanocrystals covered with a monolayer of Pd resemble those from the corresponding bulk Pd single crystals in 0.1 M HClO₄. FAO on the monolayer Pd-coated Au nanocrystals showed peak shapes in the cyclic voltammograms similar to those of bulk Pd single crystals and Pd film-covered bulk Au single crystals. FAO and CO oxidation were also conducted on Au nanocrystals covered with Pd films with increasing

thickness up to 10 MLs. The results show that the FAO peak current density and CO oxidation onset potential decreased with increasing Pd film thickness. These observations were explained with the strain and ligand effects from the d-band theory. This study demonstrates that depositing catalytically active materials as a thin film on facet-controlled nanocrystals is an effective means of obtaining high-performance catalysts because it combines the advantages of optimizing the d-band position by the substrate and the facet-dependent catalytic activity of the overlayer.

2. Experimental Section

2.1. Materials

Hydrogen tetrachloroaurate(III) trihydrate ($\text{HAuCl}_4 \cdot 3\text{H}_2\text{O}$) (99.9%), silver nitrate (AgNO_3) ($\geq 99.0\%$), sodium borohydride (NaBH_4) ($\geq 99\%$), potassium bromide (KBr) ($\geq 99.0\%$), cetyl trimethylammonium bromide (CTAB) ($\geq 98\%$), and cetylpyridinium chloride (CPC) (99.0%) were purchased from Sigma-Aldrich. L-Ascorbic acid (AA) (99%) was obtained from Acros Organics. Formic acid (88%) was obtained from Pharmco. Sodium hydroxide (98.5%), and hydrochloric acid (36.5–38%), were received from Fisher Scientific. Double-distilled perchloric acid (70%) and sulfuric acid (95–98%, ultra trace metal grade) were from GFS. Carbon monoxide (99.997%) was from Airgas. All of the chemicals were used without further purification. Ultrapure water from a Milli-Q system (18.2 $\text{M}\Omega\text{-cm}$) was used in this work.

2.2. Synthesis of Au Seeds

The synthesis of 38 nm Au seed followed previously reported multi-step methods by others with some modifications [29–32]. First, 125 μL of 10 mM HAuCl_4 was added to 5 mL of 100 mM CTAB solution at room temperature (22 ± 1 °C), followed by the addition of 300 μL of 10 mM ice-cold NaBH_4 . The mixture was stirred for 5 min and stored at room temperature for further uses. Second, 24 μL of the above solution was added to a mixture of 20 mL of 100 mM CTAB solution, 1 mL of 10 mM HAuCl_4 , 120 μL of 10 mM AgNO_3 , and 160 μL of 100 mM ascorbic acid. The solution was kept at room temperature for 2 h without stirring. The Au nanoparticles were centrifuged at 6500 rpm and redispersed in 20 mL of 100 mM CTAB. Third, 1 mL of 10 mM HAuCl_4 and 200 μL of 100 mM ascorbic acid were added in sequence into the solution at 40 °C. The solution was left undisturbed for 1 h then centrifuged at 6500 rpm and redispersed in 20 mL of 10 mM CTAB solution. Lastly, 400 μL of 10 mM HAuCl_4 was added into the solution and kept undisturbed at 40 °C overnight. The obtained Au nanoparticles were washed three times with a 100 mM CPC solution by centrifugation at 6500 rpm and then redispersed in 30 mL of 100 mM CPC. The solution was marked as the Au seed solution for further uses.

2.3. Synthesis of Au Nanocrystals

The shape-controlled synthesis of Au nanocrystals mostly followed a reported method [29]. In the synthesis of cubic Au nanocrystals, 5 mL of 100 mM KBr solution, 1 mL of 10 mM HAuCl_4 solution, 150 μL of 100 mM ascorbic acid solution, and 2 mL of the Au seed solution were added into 50 mL of 100 mM CPC solution in sequence. The solution was kept at room temperature for 2 h without stirring. The obtained cubic Au nanocrystals were washed five times by centrifugation at 3500 rpm with warm water and then redispersed in 1 mL ethanol. The synthesis of octahedral Au nanocrystals is the same as that of cubes, except that no KBr was used. In the synthesis of RD Au nanocrystals, besides the fact that no KBr was used, the volume of AA with the same concentration was increased to 2 mL and the concentration of CPC was reduced to 10 mM with the same volume.

2.4. Electrochemical Measurement

For a typical measurement, a whole batch of Au nanocrystals were further washed three times with warm water and redispersed in 500 μL ethanol before electrochemical measurement. Ten microliters (10 μL) of Au nanocrystals ethanol suspension was drop-coated on a glassy carbon (GC) disk electrode and used as the working electrode. Cyclic voltammograms (CVs) and chronoamperograms (CAs) were recorded in a conventional two-compartment three-electrode glass cell using a CHI 700C electrochemical analyzer. A Pt wire served as the counter electrode and a KCl-saturated Ag/AgCl electrode was used as the reference electrode. The counter electrode and the reference electrode were in the same compartment that is separated from the working electrode compartment by a fine porous glass frit. The cell resistance was compensated for with the iR compensation function in the analyzer. Before any electrochemical measurements, the Au nanocrystals were subject to an electrochemical cleaning process, which entails electrochemical potential cycling between -0.7 to $+0.7$ V versus Ag/AgCl for 50 cycles at a scan rate of 0.5 V s^{-1} in 0.1 M NaOH . To prepare Pd-monolayer-coated Au nanocrystals, an atomic layer of Cu was first deposited by underpotential deposition (UPD) in $0.1 \text{ M H}_2\text{SO}_4 + 1 \text{ mM CuSO}_4$ solution at 0.05 V for 10 min. Then, the Cu-layer-coated Au nanocrystals were immersed in a deaerated $0.1 \text{ M HClO}_4 + 5 \text{ mM PdCl}_2$ for 20 min to replace the atomic layer of Cu. Because of the surface-limiting nature of the Cu UPD, nominally one ML of Pd is deposited after one redox replacement cycle [27,28]. By repeating this procedure, multi-monolayers of Pd were obtained. The electrochemical surface area of Pd films was measured from CO stripping charges by assuming 320, 315, and 315 $\mu\text{C cm}^{-2}$ for complete removal of a saturated CO adlayer on the Pd overlayer deposited on RD, cubic, and octahedral Au nanocrystals [33], respectively. The CO adlayer was formed by purging the gas in the solution for 5 min with the electrode potential being held at -0.10 V versus Ag/AgCl followed by 10 min N_2 purging to remove solution CO. The stripping voltammograms were recorded in 0.1 M HClO_4 , and the potential was first scanned negatively to -0.17 V and reversed. Typically, two additional cycles between -0.17 and $+0.98 \text{ V}$ were recorded after CO oxidation, but for clarity, only the CO stripping segment was shown.

2.5. Instrumentation

Scanning electron microscopy (SEM) images were obtained on a Zeiss Supra35 scanning electron microscope operating at 5 kV. High-resolution transmission electron microscopy (HRTEM) and selected-area electron diffraction (SAED) images were taken using a JEOL2100 transmission electron microscope (JEOL USA Inc., Peabody, Massachusetts, USA) operating at 200 kV. X-ray diffraction (XRD) measurements were performed on a Scintag X1 powder diffractometer (Scintag Inc., San Francisco, CA, USA) with Cu $K\alpha$ radiation ($\lambda = 0.154 \text{ nm}$) operated at 40 kV and 25 mA by step scanning with a step size of $0.02^\circ/\text{step}$. UV-Vis spectra were recorded by an Agilent 8453 spectrophotometer (Agilent, Santa Clara, CA, USA).

3. Results and Discussion

3.1. Synthesis and Characterization of Au Nanocrystals

Cubic, octahedral, and RD gold nanocrystals enclosed by $\{100\}$, $\{111\}$, and $\{110\}$ facets were synthesized following a seed-mediated growth method developed by Niu et al. with some modifications (see experimental section) [29]. The Au seeds used in this approach have a relatively large diameter ($38 \pm 4 \text{ nm}$), as shown by the SEM image in Figure S1 in the Supplementary Material. Figure 1a–c displays the SEM images of the cubic, octahedral, and RD Au nanocrystals, respectively. The shape difference of Au nanocrystals is clearly observed. The edge length of the Au nanocubes is $61.5 \pm 3.4 \text{ nm}$ (average length and standard deviation based on measurements from 100 particles). The TEM image and square SAED pattern shown in Figure 1d confirm that these Au nanocubes are enclosed by well-defined $\{100\}$ facets [34,35]. The edge lengths of Au octahedra and RD are $63.2 \pm 4.2 \text{ nm}$ and $58.7 \pm 2.8 \text{ nm}$, respectively. TEM images and SAED patterns of octahedral and RD Au nanocrystals are

presented in Figure 1e,f. The hexagonal dot array in the SAED pattern indicates that the octahedral nanocrystal is enclosed by {111} facets [35]. The RD Au nanocrystals show the elongated hexagonal dot array, which is also consistent with the reported diffraction pattern of Au single crystals along the [011] zone axis [29,36,37]. Compared to those reported in [29], the surfaces of our RDs are smoother, suggesting higher quality of the crystals.

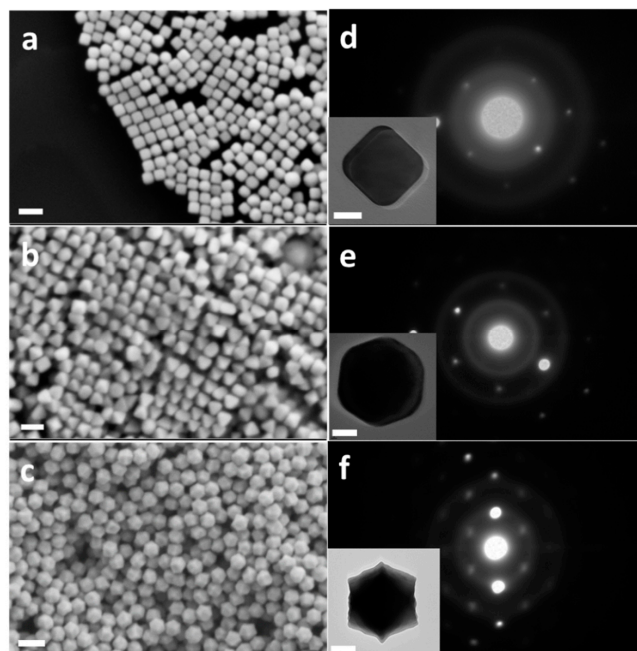


Figure 1. SEM images of (a) cubic, (b) octahedral, and (c) rhombic dodecahedral (RD) Au nanocrystals. Scale bar: 100 nm. SAED patterns of (d) cubic, (e) octahedral, and (f) RD Au nanocrystals. Inset: corresponding TEM images, scale bar: 20 nm.

The structure of the nanocrystals was further examined with powder X-ray diffraction (XRD). The cubic, octahedral, and RD Au nanocrystals show dominant (200), (111), and (220) peaks respectively, confirming the single crystal structure of these Au nanocrystals (Figure 2). The XRD pattern for RD Au nanocrystals showed a much more intense (220) peak compared to the previously reported results by others [29], suggesting that the RD Au nanocrystals synthesized in the present work have a much higher quality, which ensures more accurate activity comparison between different facets. The structural improvement may arise from the lower synthesis temperature (22 °C here versus 30 °C in [29]). Synthesizing the particles at room temperature simplifies the process by eliminating the use of temperature control devices. In addition, we increased the amount of reactants by 10 times, which produces a larger quantity of Au nanocrystals that are needed in the catalytic activity investigations.

The UV-Vis spectra in Figure S2 show shape-dependent surface plasmon resonance peaks. The peak wavelengths of cubic, octahedral, and RD Au nanocrystals are 539 nm, 559 nm, and 598 nm, respectively, which are similar to those reported in ref. 29. The differences in UV-Vis spectra mainly result from the differences in the shape of these Au nanocrystals. It is interesting to note that the peak width of the RD is significantly broader than those of cubes and octahedra. The full width at half maximum (FWHM) for RD is 110 nm, but only about 55 and 60 nm for the cubes and octahedra, respectively.

One of the advantages of the seed-mediated synthesis is that the crystal size can be conveniently tuned through varying the amount of the seed. To demonstrate this point, we decreased the volume of Au seed solution to 100 μ L in the growth step, and larger Au nanocrystals were obtained, as shown in Figure S3. The facet edges of these larger nanocrystals are easier to see compared to the smaller

ones. The size distributions of these larger cubic, octahedral, and RD Au nanocrystals are 112 ± 13 nm, 117 ± 12 nm, and 135 ± 8 nm, respectively.

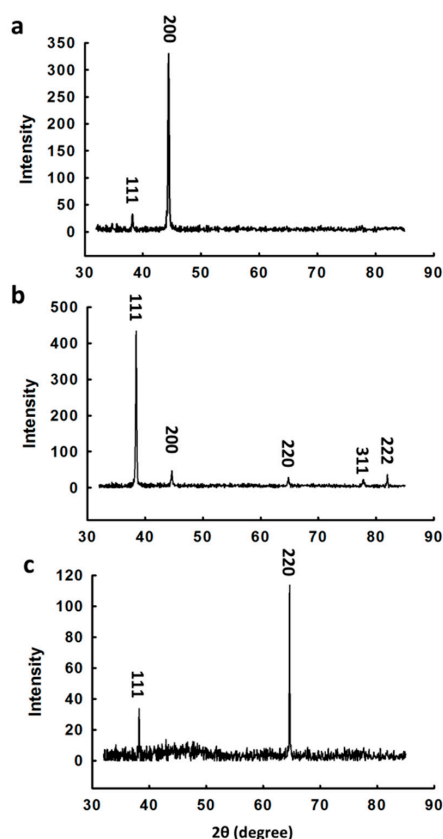


Figure 2. XRD pattern of (a) cubic, (b) octahedral, and (c) RD gold nanocrystals.

Before electrochemical studies, the residual organic adsorbates must be removed from the Au nanocrystal surfaces. This cleaning step is crucial for catalytic applications in order to obtain true shape-dependent activity [38–40]. Several methods have been developed to clean nanocrystal surfaces. However, the ozone removal method has been confirmed to cause severe surface structure distortion due to its high oxidation power [41]. Although carbon monoxide (CO) has been used for effective cleaning of surfactants on Pd nanocrystals [24,42], it does not adsorb strongly on Au surfaces [43,44]. An electrochemical fast potential cycling in a strong basic solution was used here for cleaning these Au nanocrystals, which is similar to the surfactant removal methods reported by others [39,45]. In this cleaning procedure, the as-prepared Au nanocrystals supported on a glassy carbon electrode were scanned in the potential range of -0.70 to $+0.70$ V versus Ag/AgCl at 0.5 V s^{-1} in 0.1 M NaOH for about 50 cycles until stable CVs, such as those in Figure 3a, were obtained. Before the electrochemical potential cycling treatment, the surface oxidation/reduction charge density was small and the surface oxidation current rise was sluggish as exemplified by the CV from Au nanocubes in Figure 3a (dotted trace), indicating that, even after several times of washing with water, some surfactants remained on the crystal surfaces. After the potential cycling, the surface oxidation current increased sharply between 0.2 and 0.35 V, and the surface oxidation/reduction current peaks showed facet-dependent features. The RD Au nanocrystals showed a surface oxidation peak at around 0.33 V, while on cubes it appeared at 0.4 V and two peaks located at 0.38 and 0.44 V were observed on the octahedra. On the cathodic scan, the surface oxide reduction peak of octahedra appeared at ca. 0.15 V, which is sharper and more positive than those from the cubes and RD. The adsorption peak observed around 0.0 V on the bulk Au (100) single crystal surface, which is a signature of surface reconstruction [46], was not seen on the cube surfaces, suggesting that surface reconstruction does not occur on the nanocube surfaces.

Facet-dependent voltammogram features were also observed in 0.1 M H₂SO₄ (Figure 3b), albeit the differences are more subtle than in the alkaline solutions. These voltammetric features are similar to those observed on bulk Au (111), Au (100), and Au (110) single crystal surfaces [46–48], further confirming that the nanocrystals are enclosed by the three low index facets.

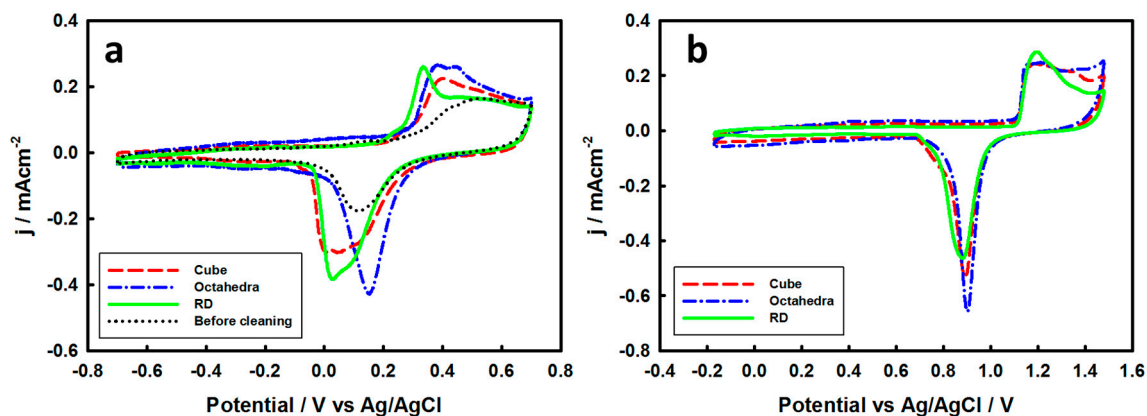


Figure 3. Cyclic voltammograms (CVs) of cubic, octahedral, and RD Au nanocrystals in (a) 0.1 M NaOH (b) 0.1 M H₂SO₄. The dotted line in (a) is the CV of cubic Au nanocrystals before the potential cycling process. Scan rate: 0.100 V s⁻¹.

3.2. Electrochemical Properties of Pd-Monolayer-Coated Au Nanocrystals

As stated in the outset, a central task in this study is to examine whether Pd thin films coated on Au nanocrystals have facet-dependent electrochemical properties, especially formic acid oxidation activity, that mimic those of bulk Pd single crystals or Pd thin film coated bulk Au single crystals [24,33,49]. After electrochemical cleaning in 0.1 M NaOH, the Au nanocrystals were coated with a layer of Pd film by the surface limited redox replacement approach, which nominally deposits one atomic layer of Pd in one deposition-replacement cycle. Figure 4a shows the CVs of different Au nanocrystals coated with a monolayer of Pd recorded in 0.1 M HClO₄. Different nanocrystals exhibited different electrochemical features both in the hydrogen adsorption/desorption and Pd oxidation/reduction regions. The Pd monolayer on cubic Au nanocrystals showed hydrogen adsorption/desorption peaks at around 0.0 V, while these peaks appeared at around -0.10 V on RD nanocrystals. A clear shoulder at ca. 0.0 V on the cathodic scan was also observed on the latter nanocrystals. These observations agree with those reported on Pd cubic and RD nanocrystals, respectively [24]. On Pd-monolayer-coated octahedral Au nanocrystals, the hydrogen adsorption/desorption peaks were more reversible than the other two crystals, in accordance with that on bulk Pd (111) single crystal electrodes [33]. At potentials above 0.40 V, a pair of redox peaks appeared at around 0.5 V on Pd-monolayer-coated Au cubes and RDs, which can be assigned to the surface oxidation/reduction of Pd on the basis of similar observations on bulk Pd (100) and (110) surfaces [33]. Interestingly, on Pd-monolayer-coated Au octahedra, the surface oxidation/reduction peaks are much smaller and less reversible, which also agree with the results from bulk Pd (111) single crystals [33,50–52], and can be explained by the relatively inert nature of the Pd {111} facet that has a much higher oxidation potential compared to the Pd {100} and Pd {110} facets [33,49]. The CO stripping voltammograms from monolayer-Pd-coated Au nanocrystals displayed in Figure 4b also show facet-dependent features. The CO oxidation peak potential for the cubic shape nanocrystals is about 50 mV more negative than the other two nanocrystals, which has been observed on Pd (100) bulk single crystal electrodes [33]. In addition to the main CO oxidation peak at 0.75 V, the octahedral nanocrystals show an additional peak at 0.9 V, which has also been observed on a bulk Pd (111) single crystal electrode [51]. The slanted voltammogram observed on the octahedra is from the background current of the supporting GC electrode and only discernable when the nanocrystal coverage is low. The similarities of the observed features in CVs and CO

stripping voltammograms between Pd-monolayer-coated Au nanocrystals and the bulk single crystal Pd electrodes/Pd nanocrystals suggest the epitaxial growth of a Pd monolayer on Au nanocrystals.

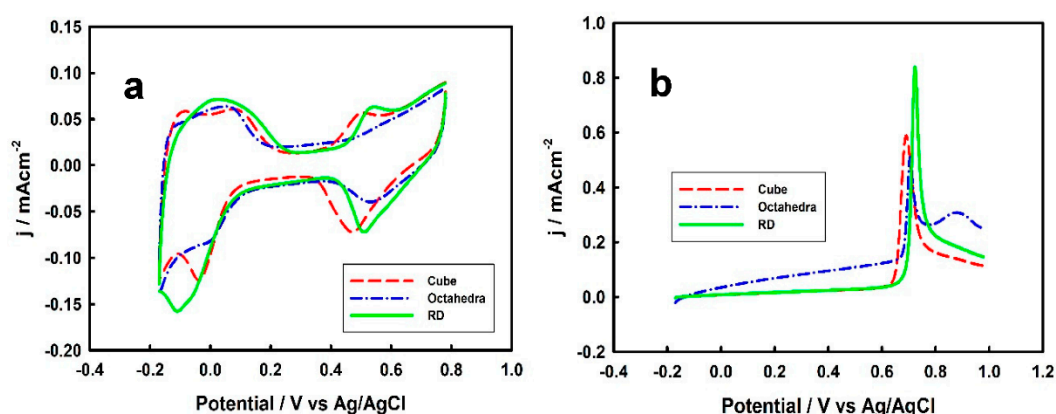


Figure 4. (a) CVs; (b) CO stripping voltammograms of cubic, octahedral, and RD Au nanocrystals coated with one monolayer of Pd recorded in 0.1 M HClO₄. Scan rate: 0.100 V s⁻¹.

Figure 5a shows CVs of FAO on Pd-monolayer-coated Au nanocrystals obtained in 0.5 M HCOOH and 0.1 M HClO₄. The FAO on these Pd monolayers exhibits shape-dependent features similar to the bulk Pd single crystal electrodes [23] and corresponding Pd nanocrystals [24,26,53]. The oxidation of formic acid on different Pd-coated Au nanocrystals started at around -0.10 V, but the monolayer Pd deposited on cubic Au nanocrystals showed the highest oxidation peak current density at about 0.4 V, which is about double that of the other two nanocrystals. On the bulk electrodes, the formic acid oxidation current density on Pd (100) is about 4 times of the other two low-index single crystal electrodes in H₂SO₄ [7], but about double that of Pd (111) in HClO₄ [23]. In addition, the CVs of Pd-monolayer-coated octahedral Au nanocrystals show similar behavior at the beginning of formic acid oxidation with cubic nanocrystals, but it reaches its maximum current at around 0.3 V, which is much more negative than that of cubic nanocrystals. The RD nanocrystals show a broader maximum current density peak at the potential range of 0.2–0.6 V. These results are consistent with the reported formic acid oxidation on different bulk Pd single crystal electrodes, in which Pd (111) showed a more negative oxidation peak potential than the other two surfaces, Pd (100) had the highest peak current density, and Pd (110) presented a broader peak [7,23]. It is interesting to note that CV features of FAO resembling those from the bulk Pd single crystals were only observed after 2 MLs of Pd deposited on the corresponding bulk Au single crystals [7]. The CVs of formic acid oxidation from these Pd-ML-coated Au nanocrystals also resemble those obtained on the corresponding Pd nanocrystals. Thus, the current density is the highest on cubic Pd nanocrystals and the peak potential is the most negative on Pd octahedra [24,26,53]. The anodic and cathodic potential scans for these Pd-ML-coated Au nanocrystals show nearly identical current densities, which signify the absence of CO poisoning on the time scale of the CV measurements.

To further compare the catalytic activity of Pd monolayers on different Au nanocrystals, formic acid oxidation current densities at 0.38 V (around the peak potential of the cubic particles) and 0.08 V read from the CVs in Figure 5a were plotted in Figure 5c,d. The plots reveal potential dependent catalytic activities of the Pd monolayers. At near peak potential (0.38 V), the Pd monolayer on cubic Au nanocrystals has the highest catalytic activity, which is more than 2 times of the other two nanocrystals. The Pd monolayer on RD nanocrystals is only slightly higher than that of octahedra. At the lower potential (0.08 V), however, the catalytic activity of the Pd monolayer deposited on RD nanocrystals is 1.5 times of the octahedral and cubic nanocrystals (Figure 5d). Moreover, the Pd monolayer on RD nanocrystals shows a better durability with 50% loss of the initial current density at 1000 s, in contrast to 70% in cubic and 90% in octahedral nanocrystals, as shown by the chronoamperometric curves (CAs) in Figure 5b. The higher durability on Pd-coated RD suggests that the surface poisoning is less

prominent on this surface at this potential. The surface poisoning species cannot be identified based solely on these results. It has been reported that, at this potential, adsorbed CO can be formed on Pd black and Pd-coated Au electrodes through electroreduction of CO₂ [21,54,55], which is a major product of FAO. It is therefore conceivable that accumulation of adsorbed CO may be responsible for the decay of the activity over time and the CO₂ reduction is structure-sensitive.

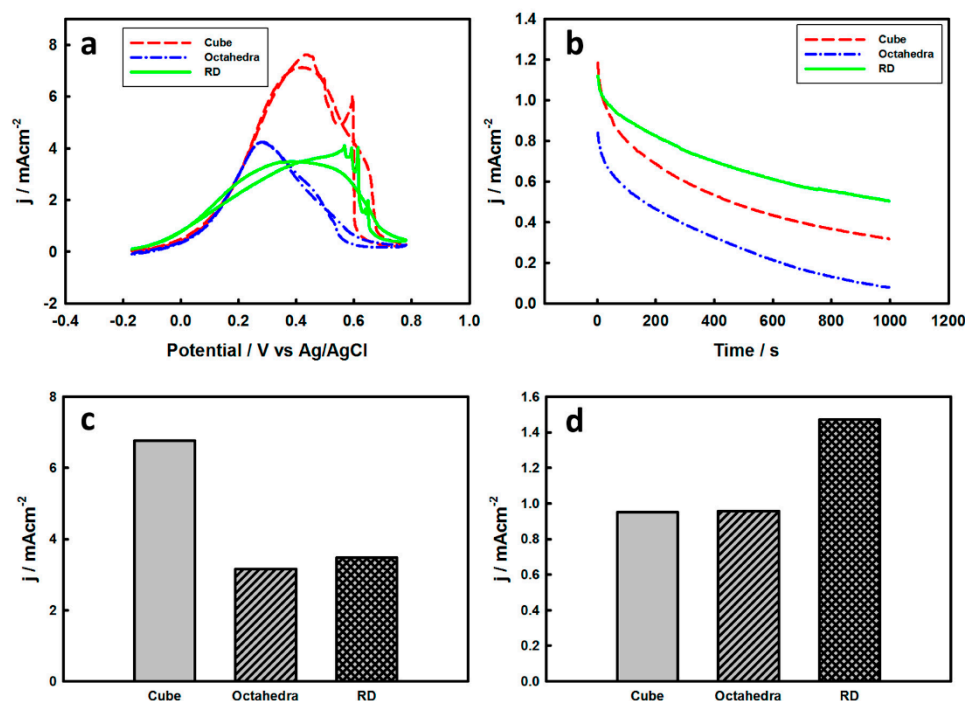


Figure 5. (a). CVs of cubic, octahedral, and RD Au nanocrystals coated with one monolayer of Pd recorded in 0.5 M HCOOH + 0.1 M HClO₄, scan rate: 0.100 V s⁻¹. (b). Corresponding chronoamperometric curves recorded in the same solution at 0.08 V with an initial potential set at -0.10 V. (c,d). Comparison of catalytic activities of Pd monolayer at (c) 0.38 V and (d) 0.08 V.

3.3. Thickness-Dependent Formic Acid Oxidation on Pd Thin Layer Coated Au Nanocrystals

The layer-by-layer growth nature of the redox replacement method for preparing the Pd films allows for the examination of film-thickness-dependent catalytic activity. We examined FAO on Au nanocrystals coated successively with up to 10 MLs of Pd. CO stripping voltammograms were recorded after the formic acid oxidation experiments to assess the electrochemically active surface area and examine Pd film thickness dependence of the CO oxidation. Figure 6 displays thickness-dependent formic acid oxidation activity in terms of current density at 0.38 V in CVs. To facilitate the comparison, the current density was normalized to that of the first layer. The error bars represent the standard deviations of results from three separately prepared Pd films. For each nanocrystal, the highest activity was observed at the first monolayer of Pd. The thickness-dependent activity of all of the nanocrystals examined followed the same trend. As the number of Pd layers increased, the formic acid oxidation activity decreased, and became largely unchanged after five monolayers of Pd. Kibler and Kolb did not observe a clear trend of thickness-dependent FAO on Pd films coated on bulk Au single crystal surfaces, but showed that the FAO current density on the first layer of Pd was in general much lower than the thicker films [7]. Similarly, Obradović and Gojković showed that the first monolayer of Pd film coated on a polycrystalline Au electrode had the lowest FAO activity, but after four monolayers of Pd, the activity remained largely the same [21]. The distinction of the first layer of Pd in the activity series between these previous studies and the present work may come from the different deposition method employed and the use of H₂SO₄ in their studies (vide infra).

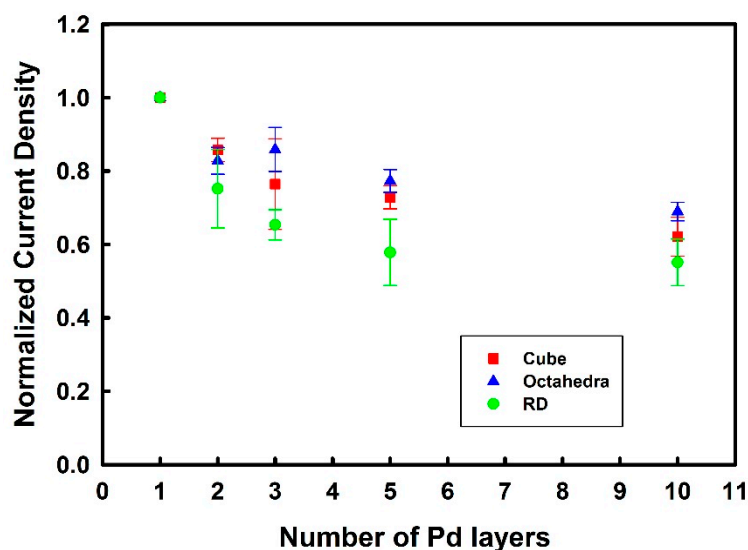


Figure 6. Normalized formic acid oxidation current density at 0.38 V as a function of the Pd film thickness measured in 0.5 M HCOOH + 0.1 M HClO₄. The error bars represent the standard deviations of results from three separately prepared Pd films.

Two effects are likely contribute to the thickness-dependent catalytic activity of these Pd overlayers on Au nanocrystals. First, the lattice constant of Au is 5% larger than that of Pd. Pseudomorphic growth of Pd on Au results in an expansion of Pd lattice, which increases the d-band center and therefore the adsorption energy of adsorbates [56]. This is the so-called strain effect. Second, the electronic interaction between two different metals results in electronic effect (the so-called ligand effect), which will cause the energy renormalization of the d-band [57]. A stronger interaction between the overlayer and the substrate atoms will result in an upshift of the d-band center of the overlayer [58]. Decoupling the two effects experimentally is challenging. In density functional theory (DFT) calculations, the two effects could be separated by artificially enlarging the lattice constant of the Pd top layer to account for the tensile strain while changing the underneath substrate from Au to Pd to eliminate the ligand effect [19,59]. All of the calculations show that the tensile strain elevates the d-band center and plays a dominant role [19,56,59,60], but there is no consensus on the ligand effect. Roudgar and Groß predicted that the ligand effect further increases the d-band center position [59], while others showed the opposite [19]. Nevertheless, the net result is an upshifted d-band center for Pd deposited on Au. As the number of Pd layers on Au nanocrystals increases, the lattice constant gradually relaxes back to the value of pure Pd, which has been demonstrated by both scanning tunneling microscopy and surface X-ray scattering [61–64]. The lattice relaxation releases the strain effect. Meanwhile, as the film thickness increases, the electronic interaction between the Pd top layer and the Au substrate becomes weaker and therefore the ligand effect diminishes. Our formic acid oxidation results are in general agreement with these arguments.

The thickness-dependent catalytic activity is also manifested in CO oxidation. Figure 7 displays CO stripping onset potential as a function of Pd overlayer thickness obtained in 0.1 M HClO₄. The onset potential here was taken as the potential where CO oxidation current is at 10% of the peak current. In the case where there are multiple peaks, the most negative peak was used. All of the three nanocrystals show a negative potential shift of CO oxidation onset potential when more than one ML of Pd was deposited. After three layers of Pd, the onset potential of CO oxidation remains largely the same. The RD nanocrystals coated with two Pd MLs showed a smaller negative shift compared with the other two Au nanocrystals. The trend of CO oxidation onset potential shift is consistent with catalytic activities shown in Figure 4 and can again be explained by the diminishing strain and ligand effects with increasing film thickness. The thickness-dependent film growth mode may be revealed from the CO stripping voltammograms (Figure S4). As the Pd film thickness increases, one obvious feature

of CO oxidation is the appearance of a second oxidation peak at around 0.9 V. This second oxidation peak was observed on octahedral nanocrystals when only one ML of Pd was deposited, but after the deposition of five MLs of Pd it can be clearly seen in all three nanocrystals, as shown in Figure S4. The second CO oxidation peak does not exist on the bulk Pd (100) and Pd (110) electrodes [50,52]. This peak might come from the defect sites formed through three-dimensional (3D) growth on the thicker Pd films, which may play a minor role in the thickness-dependent FAO activity given its smaller magnitude on the cubes and RDs.

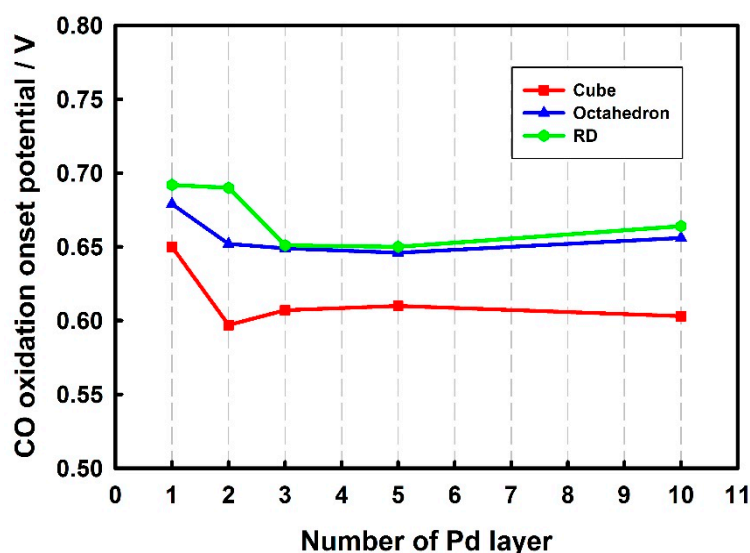


Figure 7. CO oxidation onset potential as a function of the Pd film thickness on different Au nanocrystals in 0.1 M HClO₄.

It has been demonstrated that formic acid oxidation rates are higher in HClO₄ than in H₂SO₄ [7,23,26,65], because the strong adsorption of (bi)sulfate anion on Pd surfaces above 0.2 V (versus RHE) [66,67] hinders the formic acid oxidation in H₂SO₄. It is therefore interesting to examine whether the thickness-dependent adsorption will manifest itself in (bi)sulfate adsorption and hence influences formic acid oxidation. Because of their higher catalytic activity of formic acid oxidation, Pd-film-coated cubic Au nanocrystals were chosen for this study. Figure 8 displays the formic acid oxidation current density at 0.38 V as a function of film thickness in 0.1 M HClO₄ or 0.1 M H₂SO₄ with 0.5 M formic acid. As expected, formic acid oxidation is more facile in 0.1 M HClO₄ than in 0.1 M H₂SO₄ due to the adsorption of (bi)sulfate. Interestingly, the activity disparities in the two electrolytes gradually decreased as the film thickness increased. On the first monolayer of Pd, the current density of FAO in 0.1 M HClO₄ is 1.6 times of that in 0.1 M H₂SO₄, but it decreased to only 1.2 times on 10 monolayers of Pd. This observation can be explained by thickness-dependent (bi)sulfate adsorption on Pd film surfaces. As discussed above, the d-band center upshift is the highest on the first monolayer of Pd deposited on Au nanocubes. As a result, the adsorption energy of (bi)sulfate is the strongest. The strong adsorption of (bi)sulfate anions competes with formate adsorption, and results in a lower catalytic activity compared to the nonspecifically adsorbed supporting electrolytes, such as HClO₄. This effect decreases as the thickness of the Pd film increases because the d-band center gradually returns to the value of bulk Pd. While the d-band upshift also increases the adsorption energy of formate, the effect is likely stronger on the (bi)sulfate adsorption. Given that (bi)sulfate adsorption even competes with CO adsorption on Pd [33], this assertion is not unreasonable.

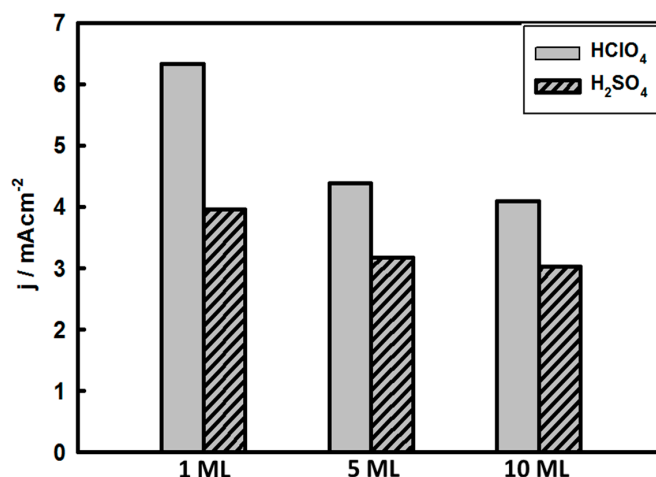


Figure 8. Formic acid oxidation current density at 0.38 V in 0.5 M HCOOH + 0.1 M HClO₄ or H₂SO₄ from cubic Au nanocrystals coated with Pd films of different thicknesses.

4. Conclusions

In summary, Pd-monolayer-covered high-quality Au nanocrystals showed facet-dependent formic acid and carbon monoxide oxidation activities that resemble those observed on bulk Pd single crystal surfaces and Pd thin film covered bulk Au single crystal surfaces, suggesting pseudomorphic growth of Pd MLs on these Au nanocrystals. As the Pd film thickness increased, the formic acid oxidation peak current density decreased and the decrement leveled off after about five MLs of Pd. Similarly, the CO oxidation onset potential also gradually decreased with the increase of Pd film thickness and remained largely unchanged after three MLs of Pd. The effects of bi(sulfate) specific adsorption on FAO also decreased with the increasing Pd film thickness. These observations are explained in terms of the d-band center shift with the Pd film thickness as a result of the tensile strain effect and the ligand effect. This study demonstrates that, by combining the facet dependence of catalytic activity with the fine-tuning of d-band position, deposition of catalytically active materials as a thin film on facet-controlled nanocrystals can be an effective approach for engineering high-performance catalysts for a variety of reactions.

Supplementary Materials: The following are available online at <http://www.mdpi.com/2571-9637/2/2/27/s1>, Figure S1: SEM image of Au seed; Figure S2: UV-Vis spectra of Au nanocrystals; Figure S3: SEM images of larger Au nanocrystals, and Figure S4: CO stripping voltammograms of Au nanocrystals coated with different layers of Pd films.

Author Contributions: Conceptualization, S.Z.; Data curation, Y.T.; Formal analysis, Y.T. and S.Z.; Funding acquisition, S.Z.; Methodology, Y.T.; Project administration, S.Z.; Supervision, S.Z.; Validation, Y.T.; Writing—original draft, Y.T.; Writing—review & editing, S.Z.

Acknowledgments: This work was partially supported by the US National Science Foundation through CHE-1156425 and CHE-1559670.

Conflicts of Interest: The authors declare no conflicts of interest.

References

- Jeong, K.-J.; Miesse, C.M.; Choi, J.-H.; Lee, J.; Han, J.; Yoon, S.P.; Nam, S.W.; Lim, T.-H.; Lee, T.G. Fuel Crossover in Direct Formic Acid Fuel Cells. *J. Power Sources* **2007**, *168*, 119–125. [[CrossRef](#)]
- Jiang, K.; Zhang, H.-X.; Zou, S.; Cai, W.-B. Electrocatalysis of Formic Acid on Palladium and Platinum Surfaces: From Fundamental Mechanisms to Fuel Cell Applications. *Phys. Chem. Chem. Phys.* **2014**, *16*, 20360–20376. [[CrossRef](#)] [[PubMed](#)]
- Uhm, S.; Lee, H.J.; Lee, J. Understanding Underlying Processes in Formic Acid Fuel Cells. *Phys. Chem. Chem. Phys.* **2009**, *11*, 9326–9336. [[CrossRef](#)]

4. Wang, X.; Hu, J.-M.; Hsing, I.M. Electrochemical Investigation of Formic Acid Electro-Oxidation and Its Crossover through a Nafion[®] Membrane. *J. Electroanal. Chem.* **2004**, *562*, 73–80. [[CrossRef](#)]
5. Yu, X.W.; Pickup, P.G. Recent Advances in Direct Formic Acid Fuel Cells (Dfacc). *J. Power Sources* **2008**, *182*, 124–132. [[CrossRef](#)]
6. Capon, A.; Parsons, R. The Oxidation of Formic Acid at Noble Metal Electrodes Part Iii. Intermediates and Mechanism on Platinum Electrodes. *J. Electroanal. Chem. Interfacial Electrochem.* **1973**, *45*, 205–231. [[CrossRef](#)]
7. Baldauf, M.; Kolb, D.M. Formic Acid Oxidation on Ultrathin Pd Films on Au(hkl) and Pt(hkl) Electrodes. *J. Phys. Chem.* **1996**, *100*, 11375–11381. [[CrossRef](#)]
8. Ha, S.; Larsen, R.; Masel, R.I. Performance Characterization of Pd/C Nanocatalyst for Direct Formic Acid Fuel Cells. *J. Power Sources* **2005**, *144*, 28–34. [[CrossRef](#)]
9. Zhu, Y.; Khan, Z.; Masel, R.I. The Behavior of Palladium Catalysts in Direct Formic Acid Fuel Cells. *J. Power Sources* **2005**, *139*, 15–20. [[CrossRef](#)]
10. Solla-Gullon, J.; Montiel, V.; Aldaz, A.; Clavilier, J. Electrochemical and Electrocatalytic Behavior of Platinum–Palladium Nanoparticle Alloys. *Electrochem. Commun.* **2002**, *4*, 716–721. [[CrossRef](#)]
11. Rand, D.A.J.; Woods, R. Determination of the Surface Composition of Smooth Noble Metal Alloys by Cyclic Voltammetry. *J. Electroanal. Chem. Interfacial Electrochem.* **1972**, *36*, 57–69. [[CrossRef](#)]
12. Antolini, E. Palladium in Fuel Cell Catalysis. *Energy Environ. Sci.* **2009**, *2*, 915–931. [[CrossRef](#)]
13. Zhou, W.; Lee, J.Y. Highly Active Core–Shell Au@Pd Catalyst for Formic Acid Electrooxidation. *Electrochem. Commun.* **2007**, *9*, 1725–1729. [[CrossRef](#)]
14. Liu, Y.; Wang, L.; Wang, G.; Deng, C.; Wu, B.; Gao, Y. High Active Carbon Supported PdAu Catalyst for Formic Acid Electrooxidation and Study of the Kinetics. *J. Phys. Chem. C* **2010**, *114*, 21417–21422. [[CrossRef](#)]
15. Zhang, G.; Wang, Y.; Wang, X.; Chen, Y.; Zhou, Y.; Tang, Y.; Lu, L.; Bao, J.; Lu, T. Preparation of Pd–Au/C Catalysts with Different Alloying Degree and Their Electrocatalytic Performance for Formic Acid Oxidation. *Appl. Catal. B Environ.* **2011**, *102*, 614–619. [[CrossRef](#)]
16. Lee, S.Y.; Jung, N.; Cho, J.; Park, H.Y.; Ryu, J.; Jang, I.; Kim, H.J.; Cho, E.; Park, Y.H.; Ham, H.C.; et al. Surface-Rearranged Pd₃Au/C Nanocatalysts by Using Co-Induced Segregation for Formic Acid Oxidation Reactions. *ACS Catal.* **2014**, *4*, 2402–2408. [[CrossRef](#)]
17. Hong, J.W.; Kim, D.; Lee, Y.W.; Kim, M.; Kang, S.W.; Han, S.W. Atomic-Distribution-Dependent Electrocatalytic Activity of Au–Pd Bimetallic Nanocrystals. *Angew. Chem. Int. Ed.* **2011**, *50*, 8876–8880. [[CrossRef](#)] [[PubMed](#)]
18. Montes de Oca, M.G.; Plana, D.; Celorrio, V.; Lazaro, M.J.; Fermín, D.J. Electrocatalytic Properties of Strained Pd Nanoshells at Au Nanostructures: CO and HCOOH Oxidation. *J. Phys. Chem. C* **2012**, *116*, 692–699. [[CrossRef](#)]
19. Celorrio, V.N.; Quaino, P.M.; Santos, E.; Flórez-Montaño, J.; Humphrey, J.J.L.; Guillén-Villafuerte, O.; Plana, D.; Lázaro, M.J.; Pastor, E.; Fermín, D.J. Strain Effects on the Oxidation of CO and HCOOH on Au–Pd Core–Shell Nanoparticles. *ACS Catal.* **2017**, *7*, 1673–1680. [[CrossRef](#)]
20. Hsu, C.; Huang, C.; Hao, Y.; Liu, F. Au/Pd Core–Shell Nanoparticles for Enhanced Electrocatalytic Activity and Durability. *Electrochem. Commun.* **2012**, *23*, 133–136. [[CrossRef](#)]
21. Obradovic, M.D.; Gojkovic, S.L. HCOOH Oxidation on Thin Pd Layers on Au: Self-Poisoning by the Subsequent Reaction of the Reaction Product. *Electrochim. Acta* **2013**, *88*, 384–389. [[CrossRef](#)]
22. Kibler, L.A.; El-Aziz, A.M.; Hoyer, R.; Kolb, D.M. Tuning Reaction Rates by Lateral Strain in a Palladium Monolayer. *Angew. Chem. Int. Ed.* **2005**, *44*, 2080–2084. [[CrossRef](#)] [[PubMed](#)]
23. Hoshi, N.; Kida, K.; Nakamura, M.; Nakada, M.; Osada, K. Structural Effects of Electrochemical Oxidation of Formic Acid on Single Crystal Electrodes of Palladium. *J. Phys. Chem. B* **2006**, *110*, 12480–12484. [[CrossRef](#)] [[PubMed](#)]
24. Zhang, H.X.; Wang, H.; Re, Y.S.; Cai, W.B. Palladium Nanocrystals Bound by {110} or {100} Facets: From One Pot Synthesis to Electrochemistry. *Chem. Commun.* **2012**, *48*, 8362–8364. [[CrossRef](#)] [[PubMed](#)]
25. Zhang, J.F.; Feng, C.; Deng, Y.D.; Liu, L.; Wu, Y.T.; Shen, B.; Zhong, C.; Hu, W.B. Shape-Controlled Synthesis of Palladium Single-Crystalline Nanoparticles: The Effect of HCl Oxidative Etching and Facet-Dependent Catalytic Properties. *Chem. Mater.* **2014**, *26*, 1213–1218. [[CrossRef](#)]
26. Zhang, X.W.; Yin, H.J.; Wang, J.F.; Chang, L.; Gao, Y.; Liu, W.; Tang, Z.Y. Shape-Dependent Electrocatalytic Activity of Monodispersed Palladium Nanocrystals toward Formic Acid Oxidation. *Nanoscale* **2013**, *5*, 8392–8397. [[CrossRef](#)]

27. Brankovic, S.R.; Wang, J.X.; Adzic, R.R. Metal Monolayer Deposition by Replacement of Metal Adlayers on Electrode Surfaces. *Surf. Sci.* **2001**, *474*, 173–179. [[CrossRef](#)]
28. Sheridan, L.B.; Kim, Y.-G.; Perdue, B.R.; Jagannathan, K.; Stickney, J.L.; Robinson, D.B. Hydrogen Adsorption, Absorption, and Desorption at Palladium Nanofilms Formed on Au(111) by Electrochemical Atomic Layer Deposition (E-ALD): Studies Using Voltammetry and in Situ Scanning Tunneling Microscopy. *J. Phys. Chem. C* **2013**, *117*, 15728–15740. [[CrossRef](#)]
29. Niu, W.; Zheng, S.; Wang, D.; Liu, X.; Li, H.; Han, S.; Chen, J.; Tang, Z.; Xu, G. Selective Synthesis of Single-Crystalline Rhombic Dodecahedral, Octahedral, and Cubic Gold Nanocrystals. *J. Am. Chem. Soc.* **2008**, *131*, 697–703. [[CrossRef](#)]
30. Nikoobakht, B.; El-Sayed, M.A. Preparation and Growth Mechanism of Gold Nanorods (NRs) Using Seed-Mediated Growth Method. *Chem. Mater.* **2003**, *15*, 1957–1962. [[CrossRef](#)]
31. Sau, T.K.; Murphy, C.J. Seeded High Yield Synthesis of Short Au Nanorods in Aqueous Solution. *Langmuir* **2004**, *20*, 6414–6420. [[CrossRef](#)] [[PubMed](#)]
32. Rodriguez-Fernandez, J.; Perez-Juste, J.; Mulvaney, P.; Liz-Marzan, L.M. Spatially-Directed Oxidation of Gold Nanoparticles by Au(III)-CTAB Complexes. *J. Phys. Chem. B* **2005**, *109*, 14257–14261. [[CrossRef](#)] [[PubMed](#)]
33. Hara, M.; Linke, U.; Wandlowski, T. Preparation and Electrochemical Characterization of Palladium Single Crystal Electrodes in 0.1 M H₂SO₄ and HClO₄ Part I. Low-Index Phases. *Electrochim. Acta* **2007**, *52*, 5733–5748. [[CrossRef](#)]
34. Kim, F.; Connor, S.; Song, H.; Kuykendall, T.; Yang, P.D. Platonic Gold Nanocrystals. *Angew. Chem. Int. Ed.* **2004**, *43*, 3673–3677. [[CrossRef](#)]
35. Seo, D.; Park, J.C.; Song, H. Polyhedral Gold Nanocrystals with O-H Symmetry: From Octahedra to Cubes. *J. Am. Chem. Soc.* **2006**, *128*, 14863–14870. [[CrossRef](#)]
36. Chen, Y.; Milenkovic, S.; Hassel, A.W. Reactivity of Gold Nanobelts with Unique {110} Facets. *ChemPhysChem* **2010**, *11*, 2838–2843. [[CrossRef](#)] [[PubMed](#)]
37. Lu, F.; Zhang, Y.; Zhang, L.; Zhang, Y.; Wang, J.X.; Adzic, R.R.; Stach, E.A.; Gang, O. Truncated Ditetragonal Gold Prisms as Nanofacet Activators of Catalytic Platinum. *J. Am. Chem. Soc.* **2011**, *133*, 18074–18077. [[CrossRef](#)] [[PubMed](#)]
38. Tian, N.; Zhou, Z.Y.; Yu, N.F.; Wang, L.Y.; Sun, S.G. Direct Electrodeposition of Tetrahedral Pd Nanocrystals with High-Index Facets and High Catalytic Activity for Ethanol Electrooxidation. *J. Am. Chem. Soc.* **2010**, *132*, 7580–7581. [[CrossRef](#)] [[PubMed](#)]
39. Vidal-Iglesias, F.J.; Aran-Ais, R.M.; Solla-Gullon, J.; Herrero, E.; Feliu, J.M. Electrochemical Characterization of Shape-Controlled Pt Nanoparticles in Different Supporting Electrolytes. *ACS Catal.* **2012**, *2*, 901–910. [[CrossRef](#)]
40. Yang, H.; Tang, Y.; Zou, S. Electrochemical Removal of Surfactants from Pt Nanocubes. *Electrochem. Commun.* **2014**, *38*, 134–137. [[CrossRef](#)]
41. Vidal-Iglesias, F.J.; Solla-Gullon, J.; Herrero, E.; Montiel, V.; Aldaz, A.; Feliu, J.M. Evaluating the Ozone Cleaning Treatment in Shape-Controlled Pt Nanoparticles: Evidences of Atomic Surface Disorder. *Electrochem. Commun.* **2011**, *13*, 502–505. [[CrossRef](#)]
42. Tang, Y.; Edelman, R.E.; Zou, S. Length Tunable Penta-Twinned Palladium Nanorods: Seedless Synthesis and Electrooxidation of Formic Acid. *Nanoscale* **2014**, *6*, 5630–5633. [[CrossRef](#)]
43. Chang, S.C.; Hamelin, A.; Weaver, M.J. Reactive and Inhibiting Adsorbates for the Catalytic Electrooxidation of Carbon-Monoxide on Gold (210) as Characterized by Surface Infrared-Spectroscopy. *Surf. Sci.* **1990**, *239*, L543–L547. [[CrossRef](#)]
44. Chang, S.C.; Hamelin, A.; Weaver, M.J. Dependence of the Electrooxidation Rates of Carbon-Monoxide at Gold on the Surface Crystallographic Orientation—A Combined Kinetic-Surface Infrared Spectroscopic Study. *J. Phys. Chem.* **1991**, *95*, 5560–5567. [[CrossRef](#)]
45. Lee, Y.; Loew, A.; Sun, S.H. Surface- and Structure-Dependent Catalytic Activity of Au Nanoparticles for Oxygen Reduction Reaction. *Chem. Mater.* **2010**, *22*, 755–761. [[CrossRef](#)]
46. Hamelin, A.; Sottomayor, M.J.; Silva, F.; Chang, S.-C.; Weaver, M.J. Cyclic Voltammetric Characterization of Oriented Monocrystalline Gold Surfaces in Aqueous Alkaline Solution. *J. Electroanal. Chem. Interfacial Electrochem.* **1990**, *295*, 291–300. [[CrossRef](#)]
47. Hamelin, A. Cyclic Voltammetry at Gold Single-Crystal Surfaces. Part 1. Behaviour at Low-Index Faces. *J. Electroanal. Chem.* **1996**, *407*, 1–11. [[CrossRef](#)]

48. Schmidt, T.J.; Stamenkovic, V.; Arenz, M.; Markovic, N.M.; Ross, P.N., Jr. Oxygen Electrocatalysis in Alkaline Electrolyte: Pt(hkl), Au(hkl) and the Effect of Pd-Modification. *Electrochim. Acta* **2002**, *47*, 3765–3776. [[CrossRef](#)]
49. Sashikata, K.; Matsui, Y.; Itaya, K.; Soriaga, M.P. Adsorbed-Iodine-Catalyzed Dissolution of Pd Single-Crystal Electrodes: Studies by Electrochemical Scanning Tunneling Microscopy. *J. Phys. Chem.* **1996**, *100*, 20027–20034. [[CrossRef](#)]
50. Zou, S.Z.; Gomez, R.; Weaver, M.J. Infrared Spectroscopy of Carbon Monoxide at the Ordered Palladium (110)-Aqueous Interface: Evidence for Adsorbate-Induced Surface Reconstruction. *Surf. Sci.* **1998**, *399*, 270–283. [[CrossRef](#)]
51. Zou, S.Z.; Gomez, R.; Weaver, M.J. Infrared Spectroscopy of Carbon Monoxide and Nitric Oxide on Palladium(111) in Aqueous Solution: Unexpected Adlayer Structural Differences between Electrochemical and Ultrahigh-Vacuum Interfaces. *J. Electroanal. Chem.* **1999**, *474*, 155–166. [[CrossRef](#)]
52. Zou, S.Z.; Gomez, R.; Weaver, M.J. Coverage-Dependent Infrared Spectroscopy of Carbon Monoxide on Palladium(100) in Aqueous Solution: Adlayer Phase Transitions and Electrooxidation Pathways. *Langmuir* **1999**, *15*, 2931–2939. [[CrossRef](#)]
53. Jin, M.S.; Zhang, H.; Xie, Z.X.; Xia, Y.N. Palladium Nanocrystals Enclosed by {100} and {111} Facets in Controlled Proportions and Their Catalytic Activities for Formic Acid Oxidation. *Energy Environ. Sci.* **2012**, *5*, 6352–6357. [[CrossRef](#)]
54. Wang, J.-Y.; Zhang, H.-X.; Jiang, K.; Cai, W.-B. From HCOOH to CO at Pd Electrodes: A Surface-Enhanced Infrared Spectroscopy Study. *J. Am. Chem. Soc.* **2011**, *133*, 14876–14879. [[CrossRef](#)]
55. Zhang, H.-X.; Wang, S.-H.; Jiang, K.; André, T.; Cai, W.-B. In Situ Spectroscopic Investigation of CO Accumulation and Poisoning on Pd Black Surfaces in Concentrated HCOOH. *J. Power Sources* **2012**, *199*, 165–169. [[CrossRef](#)]
56. Ruban, A.; Hammer, B.; Stoltze, P.; Skriver, H.L.; Nørskov, J.K. Surface Electronic Structure and Reactivity of Transition and Noble Metals. *J. Mol. Catal. A Chem.* **1997**, *115*, 421–429. [[CrossRef](#)]
57. Hammer, B.; Nørskov, J.K. Electronic Factors Determining the Reactivity of Metal Surfaces. *Surf. Sci.* **1995**, *343*, 211–220. [[CrossRef](#)]
58. Mavrikakis, M.; Hammer, B.; Nørskov, J.K. Effect of Strain on the Reactivity of Metal Surfaces. *Phys. Rev. Lett.* **1998**, *81*, 2819–2822. [[CrossRef](#)]
59. Roudgar, A.; Gross, A. Local Reactivity of Thin Pd Overlayers on Au Single Crystals. *J. Electroanal. Chem.* **2003**, *548*, 121–130. [[CrossRef](#)]
60. Shao, M.H.; Huang, T.; Liu, P.; Zhang, J.; Sasaki, K.; Vukmirovic, M.B.; Adzic, R.R. Palladium Monolayer and Palladium Alloy Electrocatalysts for Oxygen Reduction†. *Langmuir* **2006**, *22*, 10409–10415. [[CrossRef](#)]
61. Kibler, L.A.; Kleinert, M.; Kolb, D.M. Initial Stages of Pd Deposition on Au(hkl) Part II: Pd on Au(100). *Surf. Sci.* **2000**, *461*, 155–167. [[CrossRef](#)]
62. Kibler, L.A.; Kleinert, M.; Lazarescu, V.; Kolb, D.M. Initial Stages of Palladium Deposition on Au(hkl) Part III: Pd on Au(110). *Surf. Sci.* **2002**, *498*, 175–185. [[CrossRef](#)]
63. Kibler, L.A.; Kleinert, M.; Randler, R.; Kolb, D.M. Initial Stages of Pd Deposition on Au(hkl)—Part I: Pd on Au(111). *Surf. Sci.* **1999**, *443*, 19–30. [[CrossRef](#)]
64. Takahashi, M.; Tamura, K.; Mizuki, J.; Kondo, T.; Uosaki, K. Orientation Dependence of Pd Growth on Au Electrode Surfaces. *J. Phys. Condens. Matter.* **2010**, *22*, 474002. [[CrossRef](#)]
65. Vidal-Iglesias, F.J.; Arán-Ais, R.M.; Solla-Gullón, J.; Garnier, E.; Herrero, E.; Aldaz, A.; Feliu, J.M. Shape-Dependent Electrocatalysis: Formic Acid Electrooxidation on Cubic Pd Nanoparticles. *Phys. Chem. Chem. Phys.* **2012**, *14*, 10258–10265. [[CrossRef](#)]
66. Hoshi, N.; Kuroda, M.; Koga, O.; Hori, Y. Infrared Reflection Absorption Spectroscopy of the Sulfuric Acid Anion on Low and High Index Planes of Palladium. *J. Phys. Chem. B* **2002**, *102*, 9107–9113. [[CrossRef](#)]
67. Pronkin, S.; Wandlowski, T. ATR-SEIRAS—An Approach to Probe the Reactivity of Pd-Modified Quasi-Single Crystal Gold Film Electrodes. *Surf. Sci.* **2004**, *573*, 109–127. [[CrossRef](#)]

